AIP | Journal of Applied Physics

Buckling of a cantilever plate uniformly loaded in its plane with applications to surface stress and thermal loads

Michael J. Lachut and John E. Sader

Citation: J. Appl. Phys. **113**, 024501 (2013); doi: 10.1063/1.4772745
View online: http://dx.doi.org/10.1063/1.4772745
View Table of Contents: http://jap.aip.org/resource/1/JAPIAU/v113/i2
Published by the American Institute of Physics.

Buckling of a cantilever plate uniformly loaded in its plane with applications to surface stress and thermal loads

Michael J. Lachut[1] and John E. Sader[1,2,a)]
[1]*Department of Mathematics and Statistics, The University of Melbourne, Victoria 3010, Australia*
[2]*Kavli Nanoscience Institute and Department of Physics, California Institute of Technology, Pasadena, California 91125, USA*

(Received 14 September 2012; accepted 4 December 2012; published online 8 January 2013)

Buckling of elastic structures can occur for loads well within the proportionality limit of their constituent materials. Given the ubiquity of beams and plates in engineering design and application, their buckling behavior has been widely studied. However, buckling of a cantilever plate is yet to be investigated, despite the widespread use of cantilevers in modern technological developments. Here, we address this issue and theoretically study the buckling behavior of a cantilever plate that is uniformly loaded in its plane. Applications of this fundamental problem include loading due to uniform temperature and surface stress changes. This is achieved using a scaling analysis and full three-dimensional numerical solution, leading to explicit formulas for the buckling loads. Unusually, we observe buckling for both tensile and compressive loads, the physical mechanisms for which are explored. We also examine the practical implications of these findings to modern developments in ultra sensitive micro- and nano-cantilever sensors, such as those composed of silicon nitride and graphene. © *2013 American Institute of Physics*.
[http://dx.doi.org/10.1063/1.4772745]

I. INTRODUCTION

Cantilever beams and plates are used frequently in engineering applications, ranging from the boom arms of industrial cranes to flight control surfaces implemented in aviation. They also form integral components in micromechanical and nanomechanical devices.[1–35] One such application involves the atomic force microscope (AFM),[1–13] which employs a micron sized cantilever as its force sensing element. Due to their widespread use, the mechanical behavior of cantilever beams and plates has been studied extensively. The out-of-plane deflection of a cantilever transducer is analyzed in a large number of these studies, and is a cornerstone of many applications.[1–11,14–32,36–38] One important aspect that has received relatively little attention involves the coupling of in-plane loads to the out-of-plane deflection of cantilever plates. Such a mechanism can potentially lead to buckling, and is thus of particular relevance to the design of instrumentation and structures employing these devices.

Buckling of elastic beams has been examined in many studies, for which classical solutions exist. Some typical examples include the torsional buckling of thin walled bars, buckling of laterally loaded hollow beams, and buckling of columns under uniform axial forces.[40–42] The latter problem, which couples in-plane loading to the out-of-plane deflection of the beam, can be solved using Euler's column formula.[40,41] This gives the buckling load of a beam or column under varying conditions, demonstrating that boundary conditions significantly affect the overall buckling behavior.

Elastic plates have also been investigated extensively, with initial studies focusing on plates that are simply supported along all edges and under uniform compression in one direction.[40–44] Approximate solutions for loading in two orthogonal directions,[40,42,45] as well as linearly varying boundary traction for clamped or simply supported plates, have also been presented.[46–50] Subsequent developments[50–54] considered various load types such as concentrated edge loads on cantilever plates and plates subjected to nonlinear boundary loads. Interestingly, one study applied uniform compressive and tensile loads in two orthogonal directions.[42] While compressive loads were found to cause buckling, any tension in the plate resisted buckling. The higher degree of freedom associated with plates, thus, leads to an elevated level of complexity in analysis compared to beams.

In this article, we theoretically analyze the buckling behavior of a cantilever plate under an isotropic and uniform in-plane load. This situation can arise in practice from thermal and surface stress loads including, for example, loads due to molecular absorption on microcantilevers.[6–24,33,34] Importantly, the equivalent mechanical loading concept[39,44,45] does not lend itself naturally to the analysis of cantilever plates, which inherently possess mixed edge conditions. As such, we adopt the theoretical framework of Refs. 28–30, which is specifically formulated for these conditions. In Refs. 28–30, we examined the (leading-order) linear variation in stiffness of a cantilever plate due to in-plane loading. Here, we provide the essential extension of those studies to nonlinear stiffness effects, up to and including the buckling point. We show that cantilever plates can buckle under both compressive and tensile loads, which contrasts to elastic beams that only buckle under compression. Furthermore, we find that the buckling strain load has a squared dependence on the thickness-to-width ratio, and is approximately independent of the aspect ratio (length/width) and

a)E-mail address: jsader@unimelb.edu.au.

Poisson's ratio of the plate. The underlying physical mechanisms leading to this behavior are explored.

We commence our investigation by reviewing the theoretical framework of Refs. 28–30, while summarizing all key assumptions. A scaling argument based on the small deflection theory of thin plates is then presented. This yields a preliminary understanding of this buckling problem and allows for subsequent analysis of numerical results. A numerical solution is then obtained using a full three-dimensional finite element analysis (FEA).[55] This includes full stress distributions, buckling loads, and mode shapes. An analytical formula valid for arbitrary plate dimensions is also presented. Finally, the practical implications of the derived model are discussed, particularly in the context of modern developments in nanomechanical cantilever sensors.

II. THEORETICAL FORMULATION

A theoretical formalism to investigate the buckling behavior of thin cantilever plates under isotropic in-plane stress loads is now presented; see Fig. 1(a). This is based on the small deflection theory of thin plates, which allows decoupling of the in-plane stress problem from the out-of-plane deflection of the cantilever plate.[44,56,57] The following formulation builds upon the approach of Refs. 28–30, which uses small deflection theory to investigate the linear effect of surface stress on the stiffness of thin elastic plates.

To begin, we consider the related problem where the clamp is removed from the cantilever, i.e., a plate of identical geometry to the original cantilever problem but with all edges free; see Fig. 1(b). In the presence of an isotropic and

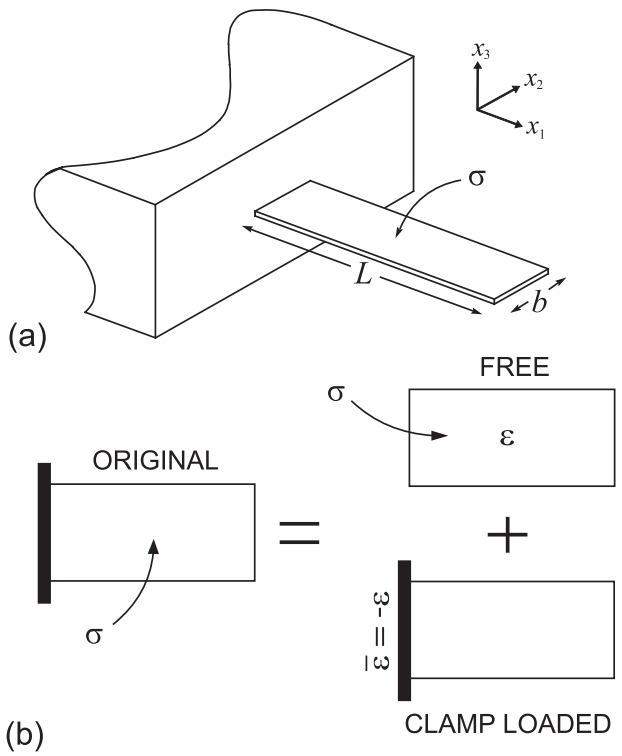

FIG. 1. Schematic of (a) cantilever plate showing coordinate system and applied in-plane load. Origin of coordinate system is at center of mass of the clamped end of the cantilever plate. (b) Decomposition of original problem, shown in the x_1-x_2 plane. Cantilever is of length L, width b, and thickness h.

uniform in-plane stress load, σ, the unrestrained plate will deform uniformly in its plane with a compatible isotropic and uniform strain, ε. Since thin plates are considered throughout, deformations in the x_3-direction are ignored. The corresponding in-plane displacement field is then given by

$$\mathbf{u} = u\hat{\mathbf{x}}_\mathbf{1} + v\hat{\mathbf{x}}_\mathbf{2} = \varepsilon(x_1\hat{\mathbf{x}}_\mathbf{1} + x_2\hat{\mathbf{x}}_\mathbf{2}), \tag{1}$$

where u, v, $\hat{\mathbf{x}}_\mathbf{1}$, and $\hat{\mathbf{x}}_\mathbf{2}$ are the displacements and unit vectors in the x_1 and x_2-directions, respectively; this displacement field is a generalization of the result provided in Refs. 28–30 which investigated the effect of an applied surface stress load. As discussed in those studies,[28–30] the displacement field of the unrestrained plate is incommensurate with the clamp condition of the original cantilever problem, i.e., the in-plane deformation must be zero at the clamp. Applying the same approach here enables decomposition of the original cantilever problem into the following two subproblems; see Fig. 1(b).

Subproblem (1): Deformation of the unrestrained plate under an arbitrary isotropic and uniform in-plane stress load σ, which gives the resulting isotropic and uniform in-plane strain ε.

Subproblem (2): Cantilever plate with no in-plane stress load σ, but with a specified in-plane displacement along its restrained edge: $u = 0$, $v = -\varepsilon x_2$. The latter condition ($v = -\varepsilon x_2$) is equivalent to applying a strain load, $\bar{\varepsilon}$, equal and opposite in sign to ε at $x_1 = 0$, i.e., $\bar{\varepsilon} = -\varepsilon|_{x_1=0}$.

Superposition of the in-plane deformations from these two subproblems yields an in-plane deformation identical to the original cantilever problem. This approach thus ensures that all boundary conditions of the original cantilever problem are satisfied. Note that the in-plane stress distribution is independent of the out-of-plane motion of the plate.[44,56,57]

Since subproblem (1) is unrestrained, the net in-plane stress in the original cantilever problem is captured by subproblem (2). As such, performing a stability analysis on subproblem (2) yields the buckling behavior of the original cantilever problem. This stability analysis extends the results of Refs. 29 and 30, by accounting for nonlinear stiffness effects due to modification of the out-of-plane deflection function by the in-plane load, i.e., cantilever stiffness is now a nonlinear function of the applied in-plane load. This allows the buckling loads and mode shapes to be rigorously determined.

Subproblem (2) is solved numerically using finite element analysis in Sec. IV.

A. Scaling analysis

A scaling analysis of subproblem (2) for an arbitrary in-plane strain load $\bar{\varepsilon}$ is now presented, for loads in the vicinity of buckling. This is to gain initial insight into the buckling behavior and enable generalization of the numerical results to cantilever plates of arbitrary dimensions.

We begin with some general considerations based on the (two-dimensional) governing equation for the small deflection of a thin plate, subject to an arbitrary in-plane load

$$D\frac{\partial^2}{\partial x_i\,\partial x_i}\left(\frac{\partial^2 w}{\partial x_j\,\partial x_j}\right) - N_{ij}\frac{\partial^2 w}{\partial x_i\,\partial x_j} = q, \tag{2}$$

where w is the deflection in the z-direction, $D \equiv Eh^3/(12[1-\nu^2])$ is the flexural rigidity, E, ν, and h are the Young's modulus, Poisson's ratio, and cantilever thickness, respectively, N is the in-plane stress tensor, and q is the applied load per unit area.

The strain load of subproblem (2) induces localized nonzero in-plane stresses in the vicinity of the clamp. These stresses decay along the major axis of the cantilever, with a characteristic length scale given by the cantilever width b, i.e., nonzero in-plane stresses are confined near the clamp ($x_1 \lesssim b$) – the in-plane stress obeys the scaling relation $N \sim O(\bar{\varepsilon}Eh)$. It then follows from Eq. (2) that since N is nonzero in the vicinity of the clamp, the effective flexural rigidity near the buckling point approaches zero only in the region $x_1 \lesssim b$. For $x_1 \gtrsim b$, where the flexural rigidity is unaffected, the cantilever behaves as a rigid body due to the relative difference in its rigidity between both regions, provided $L/b \gg 1$, where L is the cantilever length. Consequently, as the rigidity approaches zero near the clamp, the stiffness of the cantilever approaches zero at any position away from the clamp, i.e., $x_1 \gtrsim b$. The buckling load will therefore be independent of aspect ratio L/b. The buckling strain load $\bar{\varepsilon}_{\mathrm{cr}}$ for subproblem (2) is obtained by balancing the first and second terms on the left hand side of Eq. (2), giving

$$\bar{\varepsilon}_{\mathrm{cr}} \sim O\left(\left[\frac{h}{b}\right]^2\right), \tag{3}$$

valid for cantilevers of high aspect ratio, i.e., $L/b \gg 1$. Equation (3) shows that decreasing the cantilever thickness, h, reduces the buckling load, as expected.

As will become evident in Sec. IV, buckling under tensile and compressive in-plane loads exist and their respective mechanisms will be discussed. Results will also be given for the principal stress distributions and buckled mode shapes.

III. SOME PRACTICAL CASES

Before presenting these numerical results, some practical examples where an isotropic and uniform in-plane stress load σ exists are discussed:

(i) Uniform and isotropic surface stress change in the plan view faces of the cantilever plate. The corresponding strain load $\bar{\varepsilon}$ for subproblem (2) is

$$\bar{\varepsilon} = \frac{(1-\nu)\sigma_s^T}{Eh}, \tag{4}$$

where σ_s^T is the sum of surface stress changes on the upper and lower faces of the plate,[15,28–30,58] which is complimentary to the commonly characterized differential surface stress.[4,5,14,15,59]

(ii) Uniform temperature change in the entire cantilever plate/clamp structure, which gives rise to the strain load for subproblem (2)

$$\bar{\varepsilon} = -\alpha\Delta T, \tag{5}$$

where $\alpha \equiv \alpha_{\mathrm{cant}} - \alpha_{\mathrm{clamp}}$ is the differential coefficient of linear thermal expansion between the cantilever and clamp materials, α_{cant} and α_{clamp} are the coefficients of linear thermal expansion for the cantilever and clamp, respectively, $\Delta T \equiv T - T_0$ is the temperature change relative to the original reference temperature T_0 of the cantilever/clamp system, and T is the final temperature.[39,44]

Throughout, it is implicitly assumed that the cantilever plate is constructed such that if no load was applied, and the clamp was removed, the plate would not deform, i.e., the cantilever is formed in an equilibrium state. This implicit requirement is evident from the above formulation. A cantilever with inbuilt stress can also be analyzed – knowledge of this stress is required and must be added to the above specified loads.

The effect of the above loads on the buckling behavior of some cantilever devices found in practice is explored in Sec. V. Other practical examples where in-plane stress loads can be applied include piezoelectric and magnetoelastic loads.[24,32,60]

IV. RESULTS AND DISCUSSION

In this section, we solve subproblem (2) for an arbitrary strain load $\bar{\varepsilon}$. Large strain loads in particularly are considered, allowing for buckling of the cantilever plate. Large strain loads are defined as those that induce significant coupling of the in-plane stress to the out-of-plane deflection of the cantilever plate. The resulting change in the out-of-plane deflection function is rigorously and explicitly accounted for in the following analysis. This is performed using the theory of linear elasticity, in line with the theoretical framework developed in Sec. II; the effects of nonlinear elasticity are not considered.

To obtain numerical results for subproblem (2), the three-dimensional FEA[55] used in Refs. 28–30 is implemented. The mesh is systematically refined to ensure the numerical data converges to 98% accuracy. Numerical results corresponding to width-to-thickness ratios between $16 \leq b/h \leq 96$, aspect ratios in the range $2 < L/b \lesssim 16$ and Poisson's ratios over the practical range $0 \leq \nu \leq 0.49$, are presented.

Stiffness change in the cantilever problem of subproblem (2) can be examined using two equivalent approaches:[28–30] (i) monitor the change in resonant frequency or (ii) apply a fixed uniform load at the free end of the cantilever and observe changes in the static deflection; this subsequently allows for calculation of changes in the cantilever spring constant, k. The former approach is most commonly implemented in practice when small changes in stiffness are interrogated experimentally. This was the chosen approach in Refs. 28 and 29 and we reported the results of both approaches in Ref. 30. Here, we provide results for the static deflection only, since both approaches are equivalent and this facilitates identification of the buckled mode shape using the FEA software implemented.

A. Solution to subproblem (2)

As the strain load $\bar{\varepsilon}$ for subproblem (2) increases from zero, the in-plane stress initially does not affect the out-of-

plane deflection function. However, from Eq. (2), it is clear that coupling between the in-plane stress N and out-of-plane deflection function w is present at larger loads, and leads to significant modification of the deflection function.[44] Thus, in contrast to small loads which induce a linear stiffness change,[28–30] larger loads yield a nonlinear change in stiffness as the load $\bar{\varepsilon}$ is varied. This stiffness change increases rapidly in the vicinity of the buckling point. Since this is the regime where the scaling analysis presented in Sec. II A is valid, a formula for the buckling strain load $\bar{\varepsilon}_{cr}$ immediately follows from Eq. (3)

$$\bar{\varepsilon}_{cr} = \psi(\nu)\left(\frac{h}{b}\right)^2, \tag{6}$$

where $\psi(\nu)$ is a dimensionless function purely dependent on Poisson's ratio ν.

Equation (6) predicts that the buckling load $\bar{\varepsilon}_{cr}$ exhibits three key features: (i) independence of aspect ratio L/b, (ii) proportionality to the thickness-to-width ratio squared, i.e., $(h/b)^2$, and (iii) dependence on Poisson's ratio, ν. We remind the reader that Eq. (6) is derived for a cantilever of large aspect ratio, i.e., $L/b \gg 1$. These predictions are now examined using finite element analysis, in the vicinity of buckling.

We first examine dependence of the buckling strain load on aspect ratio L/b. Figure 2 gives numerical FEA results for the stiffness change $\Delta k/k_0$ as a function of the strain load $\bar{\varepsilon}$, for various aspect ratios L/b, at a fixed width-to-thickness ratio of $b/h = 48$ and Poisson's ratio $\nu = 0.25$. Note that $\Delta k \equiv k - k_0$, where k is the stiffness in the presence of an in-plane load and k_0 is the unloaded stiffness of the cantilever.

It is clear from Fig. 2 that all results converge to the same buckling points (which occur at $\Delta k/k_0 \to -1$), regardless of aspect ratio, L/b. This confirms the prediction of Eq. (6) that buckling loads are independent of aspect ratio L/b, if the aspect ratio is large – the same qualitative feature is also observed for other width-to-thickness ratios and Poisson's ratios (results not shown). The calculations in Fig. 2 show that this result holds for $L/b \gtrsim 2$.

Interestingly, we find that buckling occurs for both positive and negative strain loads $\bar{\varepsilon}$, i.e., for both tensile and compressive stress loads σ. This contrasts to classical elastic beams that buckle under compression only. An investigation of the mechanisms giving rise to this unusual phenomenon is given in Sec. IV B 1.

Next, we explore dependence of the buckling strain on the width-to-thickness ratio, b/h, and Poisson's ratio, ν. The buckling strain, $\bar{\varepsilon}_{cr}$, is determined by varying the applied strain, $\bar{\varepsilon}$, and extrapolating these numerical results to the asymptotic limit of zero stiffness, i.e., $\Delta k/k_0 \to -1$, for various h/b. The buckling strain load $\bar{\varepsilon}_{cr}$ is then multiplied by the width-to-thickness ratio squared $(b/h)^2$, in accordance with Eq. (6). In Fig. 3(a), we present this scaled buckling strain, $(b/h)^2\bar{\varepsilon}_{cr}$, as a function of thickness-to-width ratio h/b, for various Poisson's ratios, $0 \le \nu \le 0.49$, and a fixed aspect ratio of $L/b = 25/6$. Figure 3(a) shows that the scaled buckling strain, $(b/h)^2\bar{\varepsilon}_{cr}$, has a weak dependence on h/b. This demonstrates that the scaling analysis in Sec. II A correctly captures the leading-order width-to-thickness ratio dependence of the buckling strain load $\bar{\varepsilon}_{cr}$, in the limit of small h/b. This is as expected because the presented scaling analysis is derived in the asymptotic limit $h/b \to 0$.

To determine the dimensionless function $\psi(\nu)$ in Eq. (6), for both negative and positive strain loads, the numerical data for $(b/h)^2\bar{\varepsilon}_{cr}$ are extrapolated to the zero thickness limit, i.e., $h/b \to 0$. Given that $(b/h)^2\bar{\varepsilon}_{cr}$ is approximately constant for small values of h/b, extrapolation is robust and accurate. Using this procedure, we find that $\psi(\nu)$ exhibits a nonlinear Poisson's ratio ν dependence that is well described by

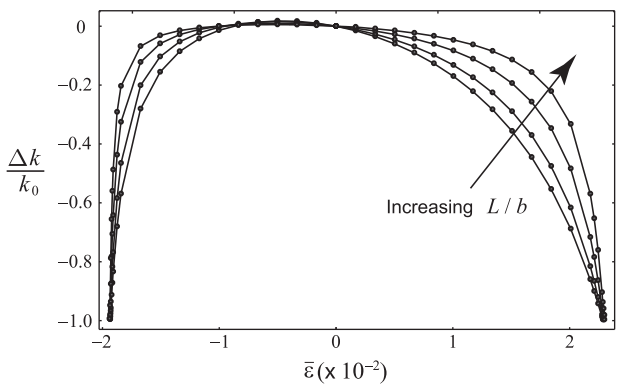

FIG. 2. Relative change in spring constant $\Delta k/k_0$ vs. strain load $\bar{\varepsilon}$. Results given for fixed width-to-thickness ratio $b/h = 48$, Poisson's ratio $\nu = 0.25$, and a range of aspect ratios of $L/b = 25/12$, $25/6$, $25/3$, and $50/3$.

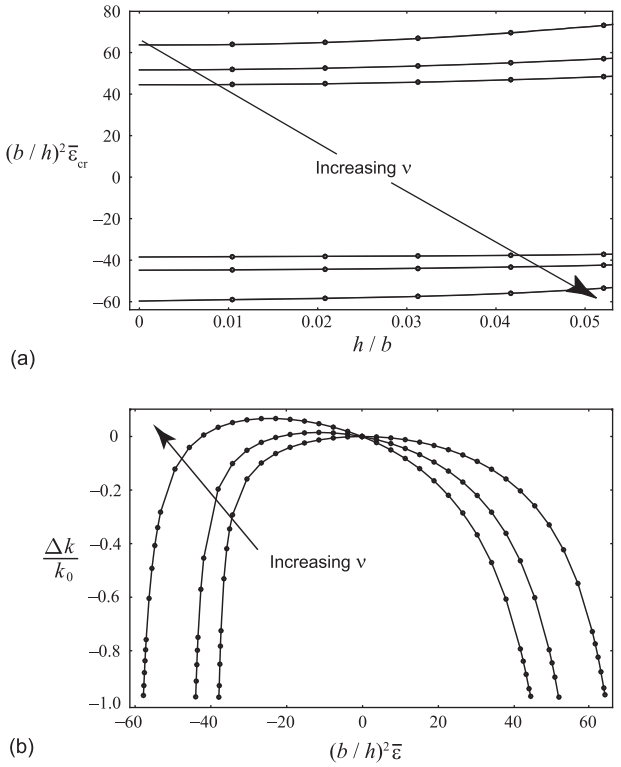

FIG. 3. Effect of Poisson's ratio, ν, on buckling behavior of a cantilever plate. Results given for an aspect ratio $L/b = 25/6$ and Poisson's ratio: $\nu = 0, 0.25$ and 0.49. (a) Scaled buckling strain load $(b/h)^2\bar{\varepsilon}_{cr}$ vs. thickness-to-width ratio h/b. Both positive and negative strain loads $\bar{\varepsilon}$ are presented. (b) Relative change in spring constant $\Delta k/k_0$ vs. scaled strain load $(b/h)^2\bar{\varepsilon}$ for a width-to-thickness ratio $b/h = 48$.

$\psi(\nu) = 63.91(1 - 0.92\nu + 0.63\nu^2)$ for $\bar{\varepsilon} > 0$, and $\psi(\nu) = -38.49(1 + 0.17\nu + 1.95\nu^2)$ for $\bar{\varepsilon} < 0$. Substituting these expressions into Eq. (6), gives the required results for the buckling loads that are valid for $L/b \gg 1$,

$$\bar{\varepsilon}_{\rm cr}^{(+)} = 63.91(1 - 0.92\nu + 0.63\nu^2)\left(\frac{h}{b}\right)^2, \tag{7a}$$

$$\bar{\varepsilon}_{\rm cr}^{(-)} = -38.49(1 + 0.17\nu + 1.95\nu^2)\left(\frac{h}{b}\right)^2, \tag{7b}$$

where $\bar{\varepsilon}_{\rm cr}^{(+)}$ and $\bar{\varepsilon}_{\rm cr}^{(-)}$ are the buckling strain loads for subproblem (2) at the buckling points for positive and negative strain loads, $\bar{\varepsilon}$, respectively.

Note that the applied strain $\bar{\varepsilon}$ in subproblem (2) and the original applied stress σ (and free strain ε) are opposite in sign. This arises from decomposition of the original problem into that for an unrestrained plate and a clamp loaded cantilever; see Sec. II and Eqs. (4) and (5). All results shall henceforth be referred to $\bar{\varepsilon}$.

Significantly, Eqs. (7) show that the buckling strain loads exhibit a weak nonlinear dependence on ν. This differs from the case of infinitesimal strain load, for which the relative change in stiffness is given by[30]

$$\frac{\Delta k_{\rm eff}}{k_0} = -0.063\nu\bar{\varepsilon}\left(\frac{b}{L}\right)\left(\frac{b}{h}\right)^2, \tag{8}$$

which possesses a strong (linear) dependence on Poisson's ratio, ν.

The mechanism leading to the weak (nonlinear) dependence of the buckling loads on Poisson's ratio ν [see Eqs. (7)] is explored in Sec. IV B 3. Equations (4), (5), and (7) are used in Sec. V to examine the practical implications of cantilever buckling due to isotropic and uniform in-plane stress loads.

Figure 3(b) shows the transition from linear to nonlinear stiffness effects, as the load $\bar{\varepsilon}$ is increased from zero, over the full range of Poisson's ratio, $0 \le \nu \le 0.49$, at a fixed aspect ratio and width-to-thickness ratio. For zero Poisson's ratio, the stiffness change is zero for small loads, i.e., $\bar{\varepsilon} \ll (h/b)^2$, as predicted by Eq. (8) and Ref. 30, but varies significantly for large loads, i.e., $\bar{\varepsilon} \sim O([h/b]^2)$. Figure 3 also reveals that the buckling strain loads decrease algebraically for both positive and negative $\bar{\varepsilon}$, as captured in Eq. (7).

In Sec. IV B, the effect of large strain loads (as defined above) on the deflection function is examined.

B. Deflection function under large strain loads

To study the effect of large strain loads ($\bar{\varepsilon} \sim O([h/b]^2)$) on the out-of-plane deflection function, we systematically increase the load from the infinitesimal limit up to the buckling point. This is performed for both positive and negative strain loads. Since the stiffness varies significantly, especially near the buckling point, the amplitude of the deflection function at the center of the cantilever free end is normalized to unity throughout. This facilitates comparison of the deflection functions under various loads.

Evolution to buckling: Figure 4 gives results for the normalized out-of-plane deflection function $W \equiv w(x_1, x_2)/$

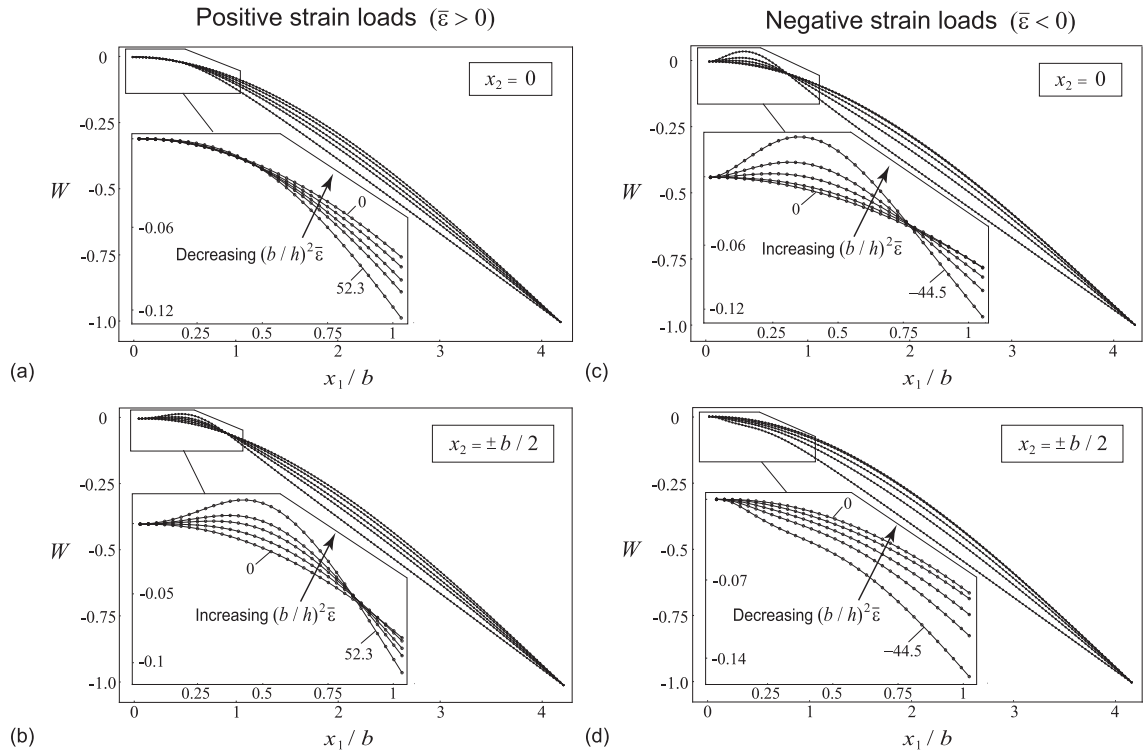

FIG. 4. Evolution of the normalized deflection function $W \equiv w(x_1, x_2)/w(L, 0)$ to the buckling point as a function of the strain load $\bar{\varepsilon}$. Positive strain loads ($\bar{\varepsilon} > 0$): (a) $x_2 = 0$; (b) $x_2 = \pm b/2$. Negative strain loads ($\bar{\varepsilon} < 0$): (c) $x_2 = 0$; (d) $x_2 = \pm b/2$. Insets are normalized deflection functions in vicinity of the clamp. Values of $(b/h)^2\bar{\varepsilon}$ shown in the insets are for zero load and the buckling loads; all values are (a) $(b/h)^2\bar{\varepsilon} = 0$, 25.6, 38.5, 44.7, 52.3; (b) $(b/h)^2\bar{\varepsilon} = 0$, −25.6, −38.5, −42.2, −44.5. Results for aspect ratio $L/b = 25/6$, width-to-thickness ratio $b/h = 48$, and Poisson's ratio $\nu = 0.25$.

$w(L,0)$, as a function of positive and negative strain loads, $\bar{\varepsilon}$. Results are given along the central axis ($x_2 = 0$) and side edges ($x_2 = \pm b/2$) of the plate. Insets show the deflection function in the vicinity of the clamp.

In Fig. 4, we observe significant modification of the deflection function as the strain load is increased from zero. Two key features are evident: (i) reduction in curvature away from the clamp ($x_1 \gtrsim b$), and (ii) non-monotonic variation in the deflection function near the clamp ($x_1 \lesssim b$). The first feature is consistent with a reduction in the flexural rigidity of the plate near the clamp only – this produces a rigid body movement away from that region. The second feature is due to strong coupling between the in-plane stresses and the deflection function. These complementary features are examined further below.

Interestingly, we observe reverse behavior in the vicinity of the clamp for positive and negative strain loads. The deflection function decreases monotonically along the central axis $x_2 = 0$ for positive strain loads, whereas this occurs at $x_2 = \pm b/2$ for negative strain loads. Similarly, non-monotonic variations occur along $x_2 = \pm b/2$ and $x_2 = 0$ for positive and negative strain loads, respectively. This reverse behavior shows that the buckled mode shapes are different for positive and negative strain loads.

Buckled mode shapes: Three-dimensional plots of the deflection functions at the buckling points, for both positive and negative strain loads, are given in Fig. 5. These results clarify the overall effect of the above mentioned variations. For positive strain loads, anticlastic curvature is observed in the mode shapes near the clamp, with the plate curling up in the x_2-direction and down in the x_1-direction; see Fig. 5(a). However, for negative strain loads [Fig. 5(c)], curvatures in both x_1 and x_2-directions are identical in sign, leading to a central bulge in the vicinity of the clamp. Away from the clamp, $x_1 \gtrsim b$, both positive and negative strain loads induce a rigid body displacement and rotation of the plate; see results in Figs. 5(b) and 5(d), which are consistent with the observations of Fig. 4. This is due to the presence of in-plane stress in the vicinity of the clamp only ($x \lesssim b$), as discussed above.

The results in Figs. 4 and 5 show that the deflection function is modified significantly near the buckling point, in comparison to the unloaded case. This modification of the deflection function gives rise to the observed nonlinear variation in stiffness, and ultimate buckling of the plate. Importantly, two distinct buckled mode shapes are found, one for positive and another for negative strain loads, $\bar{\varepsilon}$. The physical mechanisms giving rise to these different mode shapes are now examined.

1. In-plane stress distributions

Compressive stresses must exist for a structure to buckle. We, therefore, study the principal in-plane stresses in subproblem (2) to elucidate the origin of the observed buckling behavior, for both positive and negative strain loads $\bar{\varepsilon}$. The principal in-plane stresses N_1, N_2 are

$$N_1 = \frac{N_{11} + N_{22}}{2} + \sqrt{\left(\frac{N_{11} - N_{22}}{2}\right)^2 + {N_{12}}^2}, \qquad (9a)$$

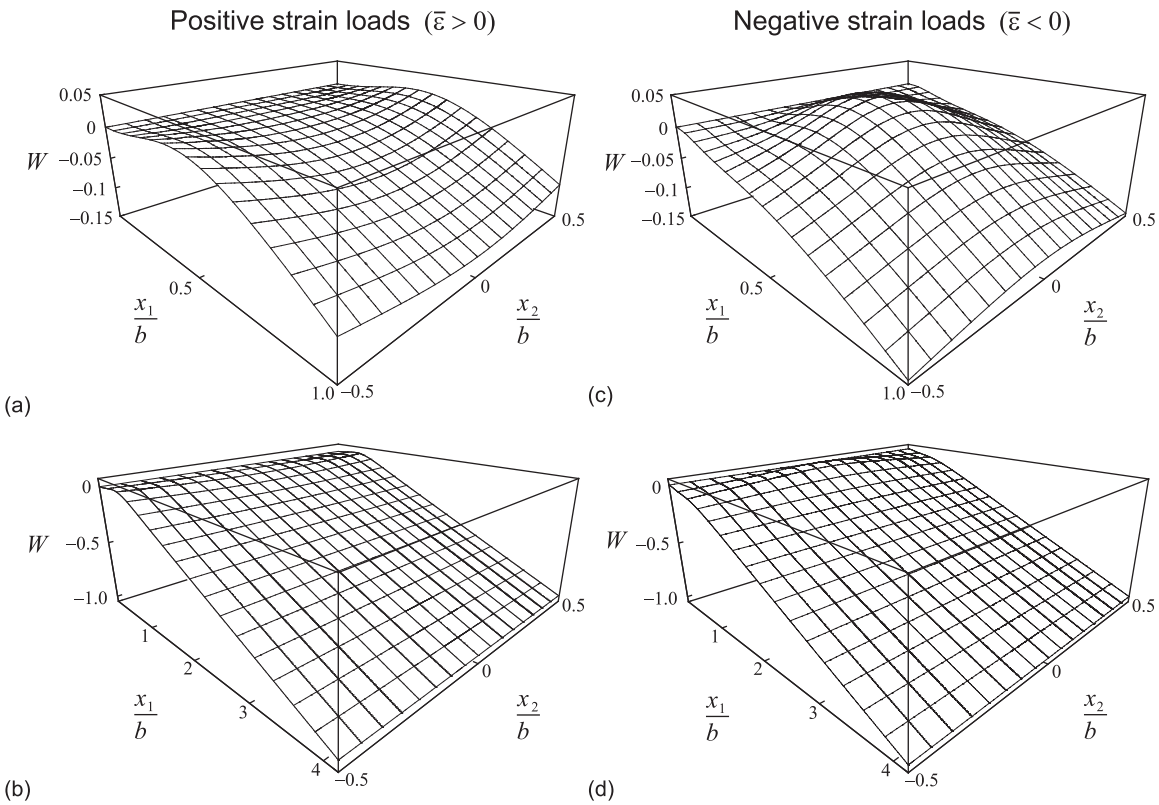

FIG. 5. Normalized buckled mode shapes $W \equiv w(x_1,x_2)/w(L,0)$ for positive and negative strain loads $\bar{\varepsilon}$. Positive strain loads ($\bar{\varepsilon} > 0$): (a) mode shape near clamp ($0 \le x_1 \le b$); (b) global mode shape ($0 \le x_1 \le L$). Negative strain loads ($\bar{\varepsilon} < 0$): (c) mode shape near clamp ($0 \le x_1 \le b$); (d) global mode shape ($0 \le x_1 \le L$). Results given for $L/b = 25/6$, $b/h = 48$, and $\nu = 0.25$.

$$N_2 = \frac{N_{11}+N_{22}}{2} - \sqrt{\left(\frac{N_{11}-N_{22}}{2}\right)^2 + N_{12}{}^2}, \qquad (9b)$$

where N_{11}, N_{22}, and N_{12} are the components of the in-plane stress tensor, and refer to the normal and shear in-plane stresses, respectively.[39] Note that N_1 is always algebraically greater than N_2, i.e., $N_1 > N_2$ for all $\bar{\varepsilon}$.

We first consider the case of a positive strain load, i.e., $\bar{\varepsilon} > 0$. Figures 6(a) and 6(b) give results for the normalized principal stresses $\overline{N_1} \equiv N_1/(\bar{\varepsilon}Eh)$ and $\overline{N_2} \equiv N_2/(\bar{\varepsilon}Eh)$, respectively. Note that N_1 is strictly positive (tensile) throughout the domain of the plate, whereas N_2 is negative (compressive) in the vicinity of the clamp and the neighboring free edges only – N_2 is tensile away from these regions. This indicates that buckling here is initiated by regions near the side edges in the vicinity of the clamp. This will be explored further below.

For the opposite case of negative strain load ($\bar{\varepsilon} < 0$), results for the stress in Figs. 6(a) and 6(b) hold, except the values of N_1 and N_2 are switched. That is, Fig. 6(a) now corresponds to $\overline{N_2}$, whereas Fig. 6(b) becomes $\overline{N_1}$. Since $\overline{N_1}$ and $\overline{N_2}$ are scaled by the strain, $\bar{\varepsilon}$, and this is now negative, we observe that both unscaled principal stresses N_1 and N_2 are negative (compressive) in the interior of the plate, whereas only N_1 is tensile near the clamp and the side edges.

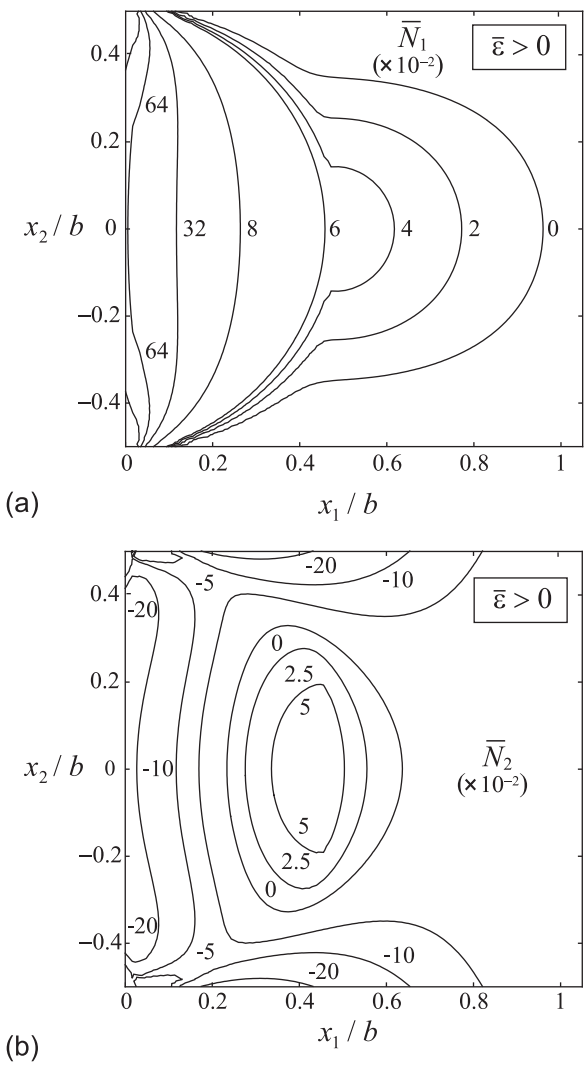

FIG. 6. Principal in-plane stress distributions for $L/b = 25/6$, $b/h = 48$, and $\nu = 0.25$. (a) Normalized principal stress $\overline{N_1} \equiv N_1/(\bar{\varepsilon}Eh)$ for $\bar{\varepsilon} > 0$; this coincides with $\overline{N_2} \equiv N_2/(\bar{\varepsilon}Eh)$ for $\bar{\varepsilon} < 0$. (b) Normalized principal stress $\overline{N_2}$ for $\bar{\varepsilon} > 0$; this coincides with $\overline{N_1}$ for $\bar{\varepsilon} < 0$.

The presence of compressive in-plane stresses for both positive and negative strain loads is consistent with buckling in both cases. However, since the compressive stress distributions differ, their buckling loads may not be identical, as observed in Fig. 2.

2. Mechanical pressure

To determine where compressive (and tensile) stresses dominate, we calculate the mechanical pressure, $P \equiv -1/2\,\mathrm{tr}\,N$. Figure 7(a) gives results for the normalized mechanical pressure, $\overline{P} \equiv P/(|\bar{\varepsilon}|Eh)$, for $\bar{\varepsilon} > 0$ with level curves divided into two regions: Regions 1 and 2, corresponding to positive and negative pressure, respectively. These results show that the pressure is positive along the side edges of the plate and away from the clamp (region 1), and there exists a central core near the clamp where the pressure is negative (region 2). The pressure is maximum at the side edges $x_2 = \pm b/2$ and in the vicinity of the clamp, near $x_1 = b/3$.

These results are to be compared to the corresponding mode shape at the buckling point, for positive strain loads; see Fig. 7(b). This mode shape differs significantly from the case of zero in-plane load, whose level sets are approximately parallel to the clamp, i.e., to the x_2-axis. The presence of an in-plane load modifies the deflection function of the plate, and at the buckling point leads to warping of the plate in the region of maximum compressive pressure, i.e., near $x_1 = b/3$ and $x_2 = \pm b/2$.

This contrasts to the opposite situation where the strain load is negative. This reverses the sign of the pressure in Fig. 7(a), thus producing compressive stress in region 2. The buckled mode shape in this case is given in Fig. 7(c), where we observe approximate coincidence of the maximum (positive) pressure position and a central bulge in the plate. Thus, we again find a strong correlation between the position of maximum (positive) pressure, and strong deviations in the buckling mode shape.

These results show that the buckled mode shapes differ for positive and negative strain loads, due to the different compressive stress distributions in these complementary cases.

3. Poisson's ratio dependence

The numerical results in Fig. 3 show that the buckling strain loads exhibit a weak dependence on Poisson's ratio, ν. To explain this feature, we first examine the Poisson's ratio dependence of the normalized mechanical pressure, $\overline{P}$. Figure 8 gives results for the difference between the $\overline{P}$ distributions for $\nu = 0$ and 0.49. This clearly shows that the mechanical pressure is insensitive to Poisson's ratio, with the differences being an order of magnitude smaller than the pressure itself, *cf.* Figs. 7(a) and 8.

The corresponding mode shapes for both positive and negative strain loads are presented in Fig. 9. In line with the

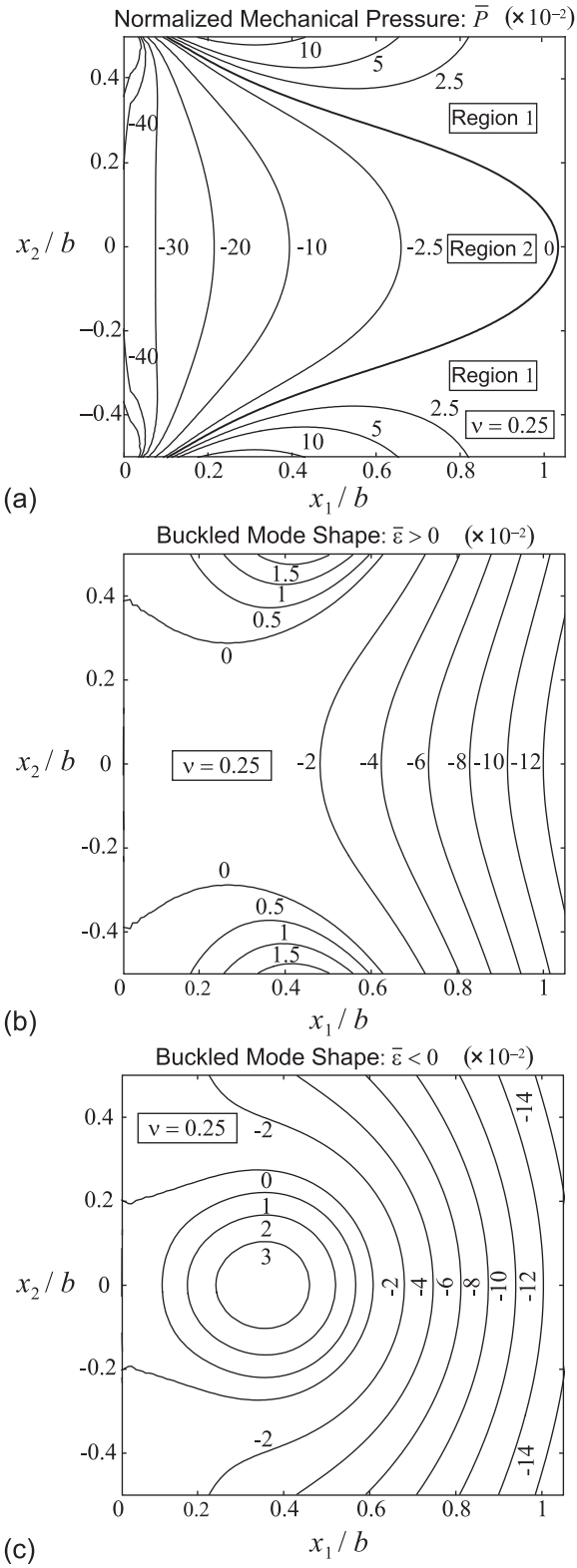

FIG. 7. Results showing connection between the mechanical pressure and the buckled mode shapes for positive and negative strain loads; for $L/b = 25/6$, $b/h = 48$, and $\nu = 0.25$. (a) Normalized mechanical pressure $\overline{P} \equiv P/(|\bar{\varepsilon}|Eh)$ for positive strain load $\bar{\varepsilon} > 0$. Normalized buckled mode shapes for (b) $\bar{\varepsilon} > 0$ and (c) $\bar{\varepsilon} < 0$. Buckled mode shapes are normalized by the displacements at the center of the cantilever free end, i.e., $x_1 = L$, $x_2 = 0$.

imposed in-plane stress distribution, we again observe identical qualitative features in the buckled mode shapes regardless of Poisson's ratio. These results show that the observed

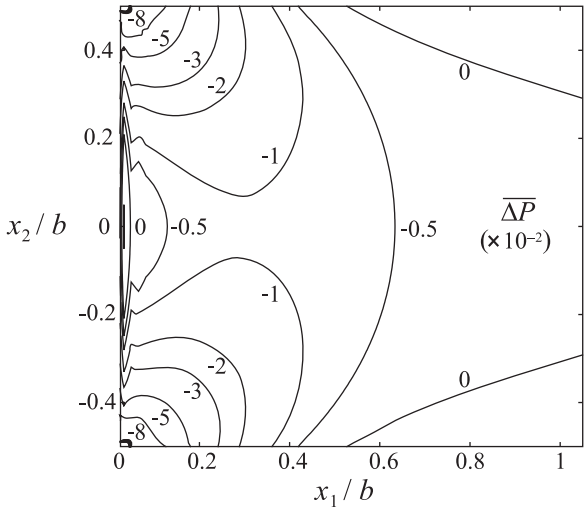

FIG. 8. Difference in the normalized mechanical pressure $\overline{P}$ for $\nu = 0$ and $\nu = 0.49$, i.e., $\overline{\Delta P} \equiv \overline{P}|_{\nu=0} - \overline{P}|_{\nu=0.49}$. Results given for $L/b = 25/6$ and $b/h = 48$.

weak dependence of the buckled mode shapes on Poisson's ratio ν is primarily due to insensitivity of the in-plane stress distribution to ν.

V. PRACTICAL IMPLICATIONS

To conclude, we explore the implications of the above findings to devices found in practice. In Sec. IV A, we derived general analytical formulas, Eq. (7), for the buckling strain loads of cantilever plates of large aspect ratio, i.e., $L/b \gtrsim 2$. These formulas are now applied to two cases of practical interest: (i) surface stress loads and (ii) thermal loads. The corresponding strain loads are given in Eqs. (4) and (5), respectively, and are used in conjunction with Eq. (7) to determine the buckling loads.

A. Surface stress loads

We first examine the effect of a change in surface stress on the buckling of some cantilevers found in practice. Importantly, Eqs. (4) and (7) show that the surface stress change, σ_s^T, required to buckle a cantilever scales linearly with its Young's modulus, E, is proportional to its thickness cubed and inversely proportional to the square of its width, i.e., $\sigma_s^T \propto Eh^3/b^2$. Thus, to increase the susceptibility of a cantilever to buckle, its thickness should be reduced and its width increased; the buckling load is independent of length, as discussed.

We consider two illustrative examples: (1) a silicon nitride cantilever $30\,\mu\text{m} \times 12\,\mu\text{m} \times 0.09\,\mu\text{m}$ from a recent study,[26] and (2) a smaller cantilever composed of multilayer graphene with dimensions $3.2\,\mu\text{m} \times 0.8\,\mu\text{m} \times 0.6$ nm,[61,62] a material which is known to behave in accordance with the continuum mechanics.[61] Reported mechanical properties for these materials and device dimensions are listed in Table I.

Silicon nitride cantilever: Using typical values for silicon nitride,[63] the surface stress loads required to buckle this device are $\sigma_s^T \approx \pm 90\,\text{N/m}$; see Table I. These values are 2-3 orders of magnitude larger than surface stress changes

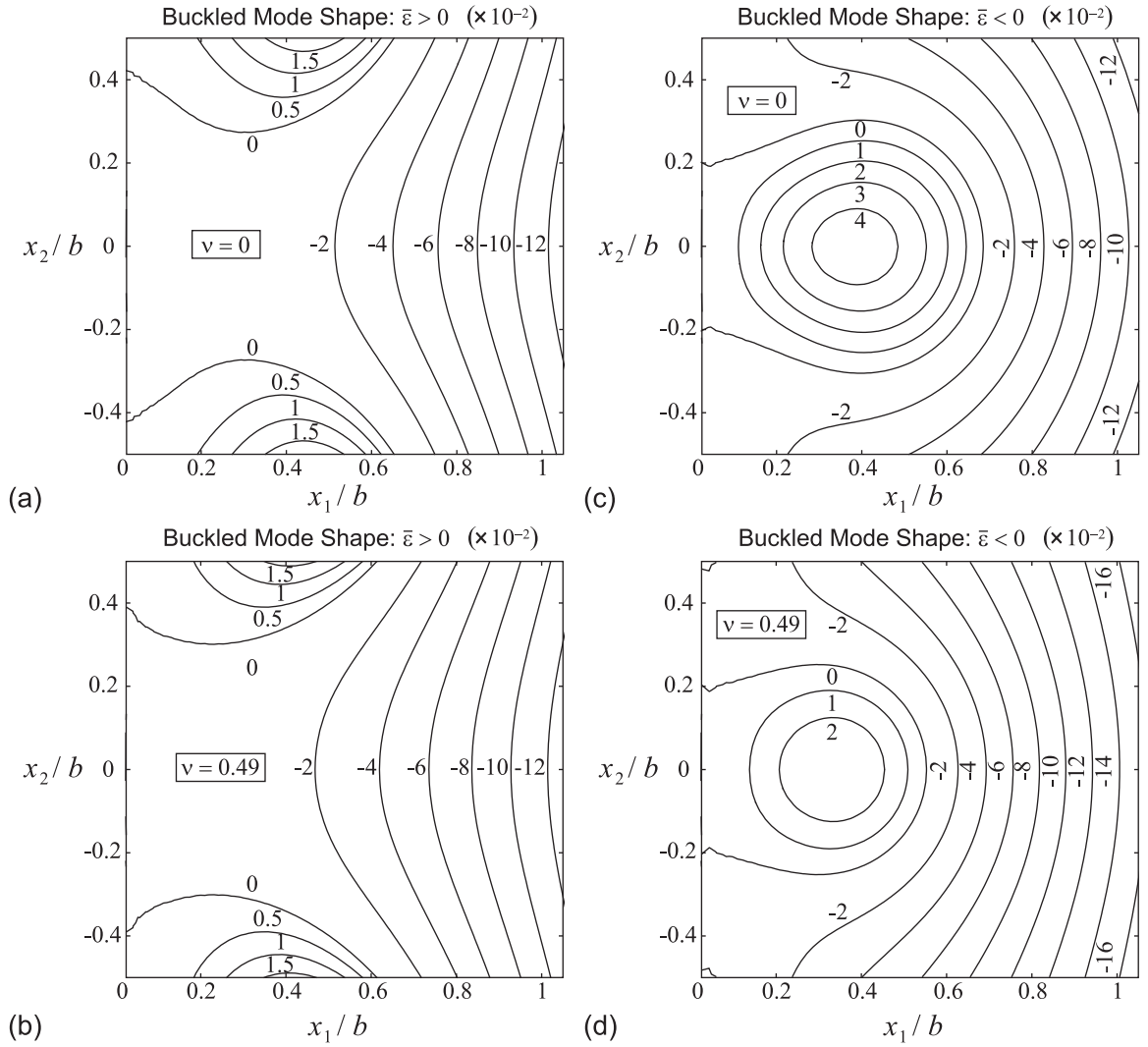

FIG. 9. Dependence of buckled mode shape on Poisson's ratio ν. Positive strain loads ($\bar{\varepsilon} > 0$): (a) $\nu = 0$; (b) $\nu = 0.49$. Negative strain loads ($\bar{\varepsilon} < 0$): (c) $\nu = 0$; (d) $\nu = 0.49$. Results given for $L/b = 25/6$ and $b/h = 48$.

typically reported.[8–10,14–16] Conventional microcantilevers used in atomic force microscopy have even larger buckling loads. This is because an increase in device size enhances the buckling loads. We therefore conclude that under practical experimental conditions, surface stress cannot buckle standard silicon nitride micro- and nano-cantilever devices.

Graphene cantilever: This device possesses a thickness two orders of magnitude smaller than the above specified silicon nitride device, which dramatically enhances it susceptibility to the effects of surface stress. In Ref. 30, we showed that such a graphene cantilever exhibits a frequency shift of $\Delta\omega/\omega_0 \approx 0.01$, for a typical surface stress change of $\sigma_s^T \approx -2.5\,\mathrm{mN\,m^{-1}}$. Using Eqs. (4) and (7), we find that a surface stress load an order of magnitude larger than this value, i.e., $\sigma_s^T \approx \pm 30\,\mathrm{mN/m}$, will buckle this device; see Table I. Importantly, this is within typically reported values for surface stress change, which are in the approximate range of 1–1000 mN/m.[8–10,14–16]

Therefore, in contrast to the above silicon nitride device, cantilevers composed of (ultrathin) graphene are highly susceptible to the effects of surface stress and may indeed be unstable under practical conditions. Typical surface stress effects at the graphene surface may therefore buckle the cantilever, thus complicating their fabrication and application.

TABLE I. Spatial dimensions (L, b, and h), material properties (ν, E, and α), surface stress changes (σ_s^T), and temperature changes (ΔT) that will buckle silicon nitride and graphene cantilevers. The difference between the linear coefficient of thermal expansion, α, of the clamp substrate and cantilever material is used to calculate the temperature change [see Eq. (5)]; the coefficient of linear thermal expansion of silicon nitride, silicon, and graphene are, respectively, 3.2, 2.6, and -0.7×10^{-6}/K.

Cantilever Material	L (μm)	b (μm)	h (nm)	ν	E (GPa)	α (10^{-6}/K)	$\sigma_s^T > 0 (< 0)$ ($\mathrm{Nm^{-1}}$)	$\Delta T > 0 (< 0)$ (K)
Si_3N_4	30	12	90	0.2	290	0.6	98.7 (−78.5)	4010 (unphysical)
Graphene	3.2	0.8	0.6	0.24	1400	−3.3	0.0324 (−0.0276)	8.9 (−7.6)

While this may present a potential limitation to the use of graphene (or similar materials) for the development of ultrasensitive sensing devices, it could also be used to advantage to construct sensors that rely on buckling phenomena.

B. Thermal loads

Next, we examine the effect of a uniform increase in temperature on the above specified devices. The substrate holding the cantilevers is taken to be silicon, which is often the practical case and for which its thermal properties are well characterized.[64] Since the silicon substrate also has a finite coefficient of thermal expansion, uniform heating of the entire cantilever/clamp structure will result in a differential stress between the cantilever and substrate, as analyzed in Sec. III. Note that if the cantilever and substrate are composed of identical materials, uniform heating cannot induce a net stress in the cantilever and hence buckling will not occur; see Eq. (5). For simplicity of discussion, we use known material properties at room temperature.

Silicon nitride cantilever: The cantilever/clamp system is assumed to be at room temperature initially. Equations (5) and (7) predict that the device will buckle when the temperature is increased by ~4000 K. Buckling cannot occur when the temperature is decreased, because the required temperature would be below absolute zero. Since the former case is above the melting point of both the clamp substrate and cantilever materials, and the latter is physically impossible, these calculations show that the device cannot buckle under thermal loads.

Graphene cantilever: The coefficient of thermal expansion α_g of a bilayer (and trilayer) of graphene was recently measured: $|\alpha_g| < 7 \times 10^{-7}$;[65] this is almost an order of magnitude smaller than that of silicon over a large temperature range. Consequently, thermal stresses in the graphene device will be induced primarily by strain in the clamp. In contrast to the silicon nitride device, we find the graphene cantilever will buckle when the temperature is varied by only $\sim \pm 8$ K; see Table I. This can be easily achieved under laboratory conditions, indicating that such ultrathin devices are highly susceptible to the effects of temperature variations. Use of a clamp substrate with a higher coefficient of thermal expansion, such as glass, will decrease the temperature change required for buckling.

Importantly, the thermal buckling load is independent of device size and relies only on (i) the thickness-to-width ratio, h/b, and (ii) the relative difference in the coefficients of linear thermal expansion between the clamp substrate and cantilever, α. Thus, a macroscopic device of similar thickness-to-width ratio, h/b, and relative coefficient of thermal expansion, α, to the above specified graphene cantilever will buckle for a similar temperature change. The same is not true for surface stress loads, whose buckling loads scale linearly with device size. These conclusions are evident from the key formulas in Eqs. (4), (5), and (7).

VI. CONCLUSIONS

We have theoretically examined the buckling behavior of thin cantilever plates that are uniformly loaded in their plane. In contrast to doubly clamped beams, we find that cantilever plates buckle under both compressive and tensile loads. This unusual feature is due to the generation of compressive in-plane stresses within the plate in both cases, which occur at different spatial regions in the vicinity of the clamp. The buckled mode shapes for positive and negative strain loads differ as a result, as do the buckling loads (albeit weakly). Importantly, since the in-plane stresses are confined to the vicinity of the clamp, the buckling loads are insensitive to variations in cantilever length, for fixed width and thickness, provided $L/b \gtrsim 2$. The buckling loads are also weakly dependent on Poisson's ratio.

The implications of this study to practical devices were also explored for surface stress and thermal loads. Typical silicon nitride micro- and nano-scale cantilevers were found to be resilient to buckling under practical conditions. This was in contrast to ultrathin devices, such as those made of graphene, which were found to buckle under both surface stress and thermal loads. This presents an opportunity to utilize the buckling behavior of nanoscale cantilever devices in the development of novel sensing applications.

ACKNOWLEDGMENTS

The authors gratefully acknowledge support of the Australian Research Council Grants Scheme.

[1]S. Boskovic, J. W. M. Chon, P. Mulvaney, and J. E. Sader, J. Rheol. **46**, 891 (2002).
[2]D. Ramos, J. Mertens, M. Calleja, and J. Tamayo, Sensors **7**, 1757 (2007).
[3]G. F. Wang and X. Q. Feng, Appl. Phys. Lett. **90**, 231904 (2007).
[4]J. E. Sader, J. Appl. Phys. **89**, 2911 (2001).
[5]J. E. Sader, J. Appl. Phys. **91**, 9354 (2002).
[6]M. Alvarez and L. M. Lechuga, Analyst **135**, 827 (2010).
[7]K. Eoma, H. S. Park, D. S. Yoonc, and T. Kwonc, Phys. Rep. **503**, 115 (2011).
[8]S. Cherian and T. Thundat, Appl. Phys. Lett. **80**, 2219 (2002).
[9]S. Cherian, A. Mehta, and T. Thundat, Langmuir **18**, 6935 (2002).
[10]A. W. McFarland, M. A. Poggi, M. J. Doyle, L. A. Bottomley, and J. S. Colton, Appl. Phys. Lett. **87**, 053505 (2005).
[11]G. Y. Chen, T. Thundat, E. A. Wachter, and R. J. Warmack, J. Appl. Phys. **77**, 3618 (1995).
[12]N. V. Lavrik, M. J. Sepaniak, and P. G. Datskos, Rev. Sci. Instrum. **75**, 2229 (2004).
[13]T. Thundat, E. A. Wachter, S. L. Sharp, and R. J. Warmack, Appl. Phys. Lett. **66**, 1695 (1995).
[14]H. Ibach, Surf. Sci. Rep. **29**, 195 (1997).
[15]P. Müller and R. Kern, Surf. Sci. **301**, 386 (1994).
[16]J. Lagowski, H. C. Gatos, and E. S. Sproles, Jr., Appl. Phys. Lett. **26**, 493 (1975).
[17]D. Ramos, M. Arroyo-Hernández, E. Gil-Santos, H. D. Tong, C. van Rijn, M. Calleja, and J. Tamayo, Anal. Chem. **81**, 2274 (2009).
[18]J. Tamayo, D. Ramos, J. Mertens, and M. Calleja, Appl. Phys. Lett. **89**, 224104 (2006).
[19]J. H. Lee, T. S. Kim, and K. H. Yoon, Appl. Phys. Lett. **84**, 3187 (2004).
[20]J. Dorignac, A. Kalinowski, S. Erramilli, and P. Mohanty, Phys. Rev. Lett. **96**, 186105 (2006).
[21]K. S. Hwang, K. Eom, J. H. Lee, D. W. Chun, B. H. Cha, D. S. Yoon, T. S. Kim, and J. H. Park, Appl. Phys. Lett. **89**, 173905 (2006).
[22]P. Lu, H. P. Lee, C. Lu, and S. J. O'Shea, Phys. Rev. B **72**, 085405 (2005).
[23]H. Duan, Acta Mech. Solida Sinica **23**, 1 (2010).
[24]R. B. Karabalin, L. G. Villanueva, M. H. Matheny, J. E. Sader, and M. L. Roukes, Phys. Rev. Lett. **108**, 236101 (2012).
[25]S. Sukuabol, D. K. Sood, and G. Rosengarten, in *Proceedings of the 2005 Intelligent Sensors, Sensor Networks & Information Processing Conference* (2005), p. 247.

[26]V. Pini, J. Tamayo, E. Gil-Santos, D. Ramos, P. Kosaka, H. D. Tong, C. van Rijn, and M. Calleja, ACS Nano **5**, 4269 (2011).
[27]A. Husain, J. Hone, H. W. C. Postma, X. M. H. Huang, T. Drake, M. Barbic, A. Scherer, and M. L. Roukes, Appl. Phys. Lett. **83**, 1240 (2003).
[28]M. J. Lachut and J. E. Sader, Appl. Phys. Lett. **95**, 193505 (2009).
[29]M. J. Lachut and J. E. Sader, Phys. Rev. Lett. **99**, 206102 (2007).
[30]M. J. Lachut and J. E. Sader, Phys. Rev. B **85**, 085440 (2012).
[31]Y. Zhang, Q. Ren, and Y.-P. Zhao, J. Phys. D: Appl. Phys. **37**, 2140 (2004).
[32]S. C. Masmanidis, R. B. Karabalin, I. De Vlaminck, G. Borghs, M. R. Freeman, and M. L. Roukes, Science **317**, 780 (2007).
[33]R. Berger, E. Delamarche, H. P. Lang, C. Gerber, J. K. Gimzewski, E. Meyer, and H. J. Guntherodt, Science **276**, 2021 (1997).
[34]D. W. Dareing and T. Thundat, J. Appl. Phys. **97**, 043526 (2005).
[35]B. Gheshlaghi and S. M. Hasheminejad, Composites, Part B **42**, 934 (2011).
[36]M. E. Gurtin, X. Markenscoff, and R. N. Thurston, Appl. Phys. Lett. **29**, 529 (1976).
[37]K. Dahmen, S. Lehwald, and H. Ibach, Surf. Sci. **446**, 161 (2000).
[38]K. Dahmen, H. Ibach, and D. Sander, J. Magn. Magn. Mater. **231**, 74 (2001).
[39]S. P. Timoshenko and J. N. Goodier, *Theory of Elasticity* (McGraw-Hill, New York, 1951).
[40]C. M. Wang, C. Y. Wang, and J. N. Reddy, *Exact Solutions for Buckling of Structural Members* (CRC, Boca Raton, 2004).
[41]C. H. Yoo and S. C. Lee, *Stability of Structures: Principles and Applications* (Elsevier, Oxford, 2011).
[42]S. P. Timoshenko and M. Gere, *Theory of Elastic Stability* (McGraw-Hill, New York, 1961).
[43]B. G. Falzon and D. Hitchings, *An Introduction to Modelling Buckling and Collapse* (NAFEMS, Glasgow, 2006).
[44]E. H. Mansfield, *The Bending and Stretching of Plates* (Pergamon, New York, 1964).
[45]R. M. Jones, Composites, Part A **36**, 1355 (2005).
[46]A. W. Leissa and J. H. Kang, Int. J. Mech. Sci. **44**, 1925 (2002).
[47]J. H. Kang, Int. J. Struct. Stab. Dyn. **1**, 527 (2001).
[48]J. H. Kang and A. W. Leissa, Int. J. Solids Struct. **42**, 4220 (2005).
[49]R. Romeo and G. Ferrero, AIAA J. **39**, 932 (2001).
[50]C. Xiang-sheng, Appl. Math. Mech. **11**, 377 (1990).
[51]C. W. Bert and K. K. Devarakonda, Int. J. Solids Struct. **40**, 4097 (2003).
[52]K. K. Devarakonda and C. W. Bert, Mech. Adv. Mater. Struct. **11**, 433 (2004).
[53]A. van der Neut, "Buckling caused by thermal stresses," in *High Temperature Effects in Aircraft Structures* (Pergamon, 1958).
[54]D. J. Gorman and R. K. Singhal, J. Sound Vib. **162**, 489 (1993).
[55]LUSAS is a trademark of, and is available from FEA Ltd. Forge House, 66 High St., Kingston Upon Thames, Surrey KT1 1HN, UK. 3D quadrilateral elements were used. Mesh was refined to 98% convergence.
[56]S. S. Rao, *Vibration of Continous Systems* (John Wiley & Sons, NJ, 2007).
[57]S. P. Timoshenko and S. Woinowsky-Krieger, *Theory of Plates and Shells* (McGraw-Hill, New York, 1959).
[58]M. E. Gurtin and A. I. Murdoch, Arch. Ration. Mech. Anal. **57**, 291 (1974).
[59]G. G. Stoney, Proc. R. Soc. Lond. A **82**, 172 (1909).
[60]S. V. Kankanala and N. Triantafyllidis, J. Mech. Phys. Solids **56**, 1147 (2008).
[61]D. B. Zhang, E. Akatyeva, and T. Dumitrică, Phys. Rev. Lett. **106**, 255503 (2011).
[62]P. Li, Z. You, and T. Cui, Appl. Phys. Lett **101**, 093111 (2012).
[63]A. Khan, J. Philip, and P. Hess, J. Appl. Phys. **95**, 1667 (2004).
[64]Y. Okada and Y. Tokumaru, J. Appl. Phys. **56**, 314 (1984).
[65]H. Conleyt, N. V. Lavrik, D. Prasai, and K. I. Bolotin, Nano Lett. **11**, 4748 (2011).